Article:

Ramadan, A.J. orcid.org/0000-0003-4572-3459, Jeong, W.H., Oliver, R.D.J. orcid.org/0000-0003-4980-7940 et al. (15 more authors) (2024) The role of the organic cation in developing efficient green perovskite LEDs based on quasi-2D perovskite heterostructures. Advanced Functional Materials, 34 (14). 2309653. ISSN 1616-301X

https://doi.org/10.1002/adfm.202309653

The Role of the Organic Cation in Developing Efficient Green Perovskite LEDs Based on Quasi-2D Perovskite Heterostructures

Alexandra J. Ramadan, Woo Hyeon Jeong, Robert D. J. Oliver, Junke Jiang, Akash Dasgupta, Zhongcheng Yuan, Joel Smith, Jae Eun Lee, Silvia G. Motti, Olivia Gough, Zhenlong Li, Laura M. Herz, Michael B. Johnston, Hyosung Choi, Jacky Even, Claudine Katan, Bo Ram Lee,* and Henry J. Snaith**

Two dimensional/three-dimensional (2D/3D) metal halide perovskite heterostructures have attracted great interest in photovoltaic and light-emitting diode (LEDs) applications. In both, their implementation results in an improvement in device efficiency yet the understanding of these heterostructures remains incomplete. In this work the role of organic cations, essential for the formation of 2D perovskite structures is unraveled, in a range of metal halide perovskite heterostructures. These heterostructures are used to fabricate efficient green perovskite LEDs and a strong dependence between cation content and device performance is shown. The crystal structure, charge-carrier transport and dynamics, and the electronic structure of these heterostructures are studied and it is shown that the presence of crystalline 2D perovskite inhibits electron injection and ultimately lowers device performance. This work highlights the importance of optimizing the composition of these heterostructures in ensuring optimal device performance across all parameters and suggests that developing routes to inject charge-carriers directly into 2D perovskite structures will be important in ensuring the continued development of perovskite LEDs based on these heterostructures.

1. Introduction

Metal halide perovskite light-emitting diodes (PeLEDs) are set to be a highly exciting new technology due to their highly efficient[1] tunable narrow emission spectra,[2] and their compatibility with low-cost fabrication processes.[3] Since initial reports,[4,5] vast increases in efficiency, stability,[6,7] and a broad range of feasible colors have been reported.[8–11] Considerable research interest has been directed to optimizing the formation of the perovskite emitter, to enhance the performance of corresponding PeLEDs. Within the broad category of thin film perovskite emitters two-dimensional/three-dimensional (2D/3D) heterostructures, hereafter referred to as quasi-2D, have been proven as a promising approach for developing highly efficient PeLEDs.[12–16] In this approach, large organic cations known

---

A. J. Ramadan, R. D. J. Oliver
Department of Physics and Astronomy
University of Sheffield
Hounsfield Road, Sheffield S3 7RH, UK
E-mail: a.ramadan@sheffield.ac.uk

A. J. Ramadan, R. D. J. Oliver, A. Dasgupta, Z. Yuan, J. Smith, J. E. Lee, O. Gough, Z. Li, L. M. Herz, M. B. Johnston, H. J. Snaith
Clarendon Laboratory
Department of Physics
University of Oxford
Parks Road, Oxford OX1 3PU, UK
E-mail: henry.snaith@physics.ox.ac.uk

The ORCID identification number(s) for the author(s) of this article can be found under https://doi.org/10.1002/adfm.202309653

DOI: 10.1002/adfm.202309653

W. H. Jeong, B. R. Lee
School of Advanced Materials Science and Engineering
Sungkyunkwan University
Suwon 16419, Republic of Korea
E-mail: brlee@skku.edu

J. Jiang, C. Katan
CNRS, ISCR – UMR 6226
Univ Rennes
ENSCR
INSA Rennes
Rennes F-35000, France

S. G. Motti
School of Physics and Astronomy
Faculty of Engineering and Physical Sciences
University of Southampton
University Road, Southampton SO17 1BJ, UK

L. M. Herz
Institute for Advanced Study
TU Munich
Lichtenbergstr. 2a, 85748 Garching, Germany

to form layered, or 2D perovskite structures (such as Ruddlesden–Popper structures) are mixed with precursors based on smaller cations known to induce a 3D perovskite (e.g. $CsPbBr_3$) and so a mixture of 2D and 3D structures are spontaneously formed in the fabrication of the perovskite emitting layer.[17,18] This approach typically results in PeLEDs with a high external quantum efficiency of electroluminescence (EQE_{EL}), the figure of merit by which we judge the performance of PeLEDs. This approach has been demonstrated to produce high efficiency PeLEDs across all colors with impressive EQE_{EL} values reported for blue (>13%),[6,19–22] green (>28%),[7,23] and red (>25%)[24,25] and near infra-red (>23%)[26,27] emission. Despite the impressive efficiencies achieved, device operational lifetime remains a key issue and the demonstrated half-life of state-of-the-art PeLEDs remains starkly lower than that of organic LEDs.[2,28] The potential sources of these instabilities are numerous ranging from inherent materials instabilities to the influence of device operation (e.g., ion migration, joule heating, etc.).[29–31] In the case of the perovskite emitting layer itself, it has been demonstrated that the quasi-2D heterostructures themselves can be catastrophic for operational PeLED stability.[32] If we are to try to overcome the instabilities of these quasi-2D heterostructures and greatly enhance their PeLED device operational stability, it is critical that we develop a comprehensive understanding of these structures, their energetic landscape, and the charge-carrier dynamics within/across them. Indeed, the recent demonstration of exceptional perovskite photovoltaic device stability through the implementation of these heterostructures is incredibly encouraging and suggests that these instabilities are not an inherent feature of these interfaces.[33,34]

In this work, we comprehensively investigate the role of organic cations within a quasi-2D perovskite emitting layer. We study the structure, charge-carrier dynamics, and energetic alignment of these heterostructures and directly correlate these properties to the performance of corresponding PeLEDs. We find that the addition of the organic cation increases PeLED performance up to a critical point. We uncover that the improved performance is largely due to a quantum confinement effect increasing the effective charge-carrier density in the 3D perovskite regions, so radiative recombination outcompetes non-radiative recombination pathways. After a critical point, when higher amounts of organic cation are introduced, the PeLED performance deteriorates rapidly which coincides with crystalline 2D perovskite being detectable with X-ray scattering measurements. From photoelectron spectroscopy and unipolar current injection measurements, we discover that the 2D perovskite introduces substantial electron-injection barriers in the perovskite material which explains the dramatic reduction in PeLED performance with high concentrations of 2D cations. Our work demonstrates that researchers need to suppress the formation of crystalline 2D perovskite and overcome electron-injection barriers to enhance the performance of quasi-2D PeLED devices.

2. Results and Discussion

To correlate significant changes in the properties of the perovskite with the influence of the organic cation, a range of different perovskite compositions were prepared with $CsPbBr_3$ employed as the 3D perovskite and the organic cation butylammonium bromide (BABr) to induce 2D perovskite formation. The resulting perovskite systems are discussed throughout with the general formula $(BABr)_x(CsPbBr_3)_{1-x}$ where the values of x were determined from the precursor molarities. Full precursor masses can be found in Table S1 (Supporting Information). The $(BABr)_x(CsPbBr_3)_{1-x}$ perovskite layers investigated in this work were fabricated through a spin-coating process and the post-deposition annealing process was based on the encapsulation growth method detailed in the work by Liu and coworkers.[12] Full details of the fabrication process can be found in the experimental methods. **Figure 1** and Figures S1 and S2 (Supporting Information) show the performance of characteristic LEDs based on the $(BABr)_x(CsPbBr_3)_{1-x}$ emitting layers. A cross-section scanning electron microscopy image of the device architecture employed in this work is shown in Figure 1a and is as follows: ITO/poly(3,4-ethylenedioxythiophene) polystyrene sulfonate (25 nm), (PEDOT: PSS)/polyvinylcarbazole (PVK) (15 nm)/perovskite (40 nm)/(1,3,5-benzinetriyl)-tris(1-phenyl-1-H-benzimadizole (TPBi) (40 nm)/LiF (1 nm)/Al (70 nm).

The electroluminescence (EL) spectra are presented in Figure 1b. As the organic cation content is increased, the EL peak position is blue shifted, as has been previously reported.[32] Across the compositional range the emission shifts from 518 nm ($x = 0.17$) to 495 nm ($x = 0.58$). In each condition, the full width at half maximum (FWHM) of the EL spectra is narrow (<30 nm, see **Table 1**), indicating good color purity of the PeLEDs. Figure 1c shows the EQE_{EL} as a function of the injected current density. A gradual increase in the peak EQE_{EL} is observed with higher amounts of organic cation. We achieved a maximum EQE_{EL} of 16.5% when 50% of BABr is incorporated in the perovskite emitters (detailed device parameters can be found in Table 1). However, a critical point in the perovskite composition emerges after which additional incorporation of BABr into the perovskite emitter begins to negatively impact the device performance (x >0.5). Figure 1d shows the voltage dependence of the current density and luminance (J–V–L) curves of representative devices for each $(BABr)_x(CsPbBr_3)_{1-x}$ composition. With increasing organic cation content, a reduction in the current density is observed which is broadly concomitant with a reduction in the luminance of the LEDs.

To understand the significant loss in device performance observed for the highest BABr content, thin films of the perovskite emissive layers were fabricated onto glass substrates and we investigated the inherent structural and morphological properties of the perovskite.

H. Choi
Department of Chemistry
Research Institute for Convergence of Basic Sciences
and Research Institute for Natural Science
Hanyang University
Seoul 04763, Republic of Korea

J. Even
Institut FOTON—UMR 6082
Univ Rennes
INSA Rennes
CNRS
Rennes F-35000, France

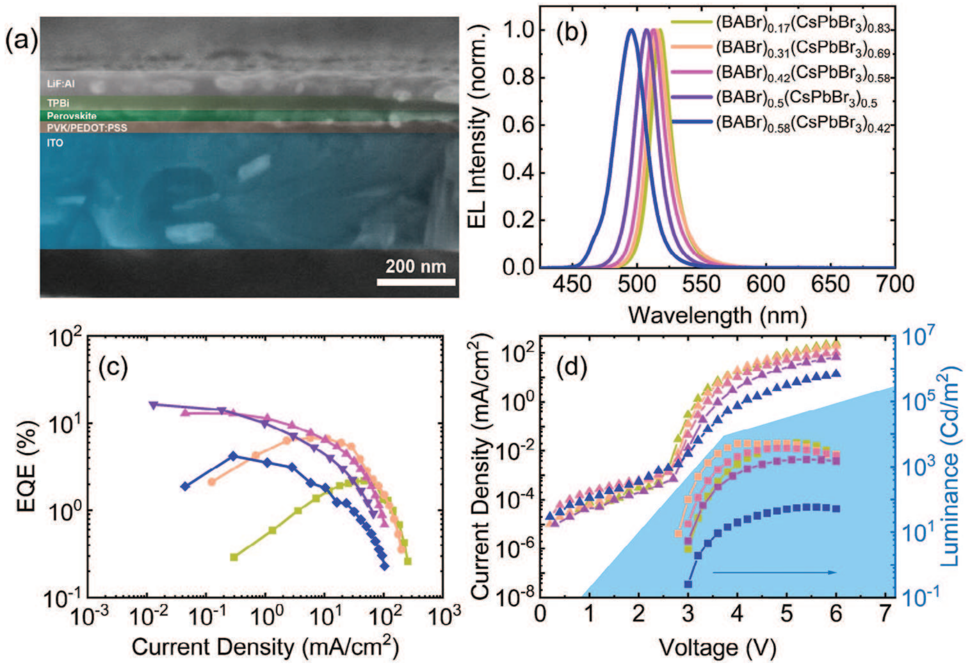

Figure 1. a) Cross-sectional scanning electron microscopy image showing the architecture of light emitting diodes based on $(BABr)_x(CsPbBr_3)_{1-x}$ and the corresponding b) electroluminescence spectra c) external quantum efficiencies with respect to current density and d) current density-voltage-luminance characteristics.

Across the compositional range explored in this work, three distinct structural regimes can be observed. **Figure** 2 shows grazing incidence wide-angle X-ray scattering (GIWAXS) 2D diffraction patterns demonstrating these regimes, patterns for other compositions can be found in Figure S3 (Supporting Information). At the lower organic cation compositions ($x = 0.17$–0.42), the structure observed matches the 3D $CsPbBr_3$ crystal structure as shown in Figure 2a where we take the $x = 0.17$ material as a representative case. At the optimal composition for maximizing PeLED EQE_{EL} (where $x = 0.5$) we find evidence of a mixed-phase film with both the $CsPbBr_3$ phase and an additional weak scattering ring at $Q \approx 0.93$ Å^{-1} ($2\theta = 13.2°$) shown in Figure 2b. Previous similar compositional series have not observed this reflection.[14,35] and whilst Cs_4PbBr_6 has previously been noted as a secondary phase in similar materials, reflections would be expected at $2\theta = 12.6$ and $12.9°$ so the origin of this peak is unclear.[36]

Finally, the composition with the highest organic cation component ($x = 0.58$) has the most starkly different structure from that of the other systems investigated in this work (Figure 2c). Here the dominant scattering is from the $n = 2$ $BA_2CsPb_2Br_7$ Ruddlesden–Popper phase, together with a few broad contributions, and a shoulder at 13.2° which is most likely from the same origin as in $x = 0.5$ (a comparison is given in Figure 2d). The $n = 2$ structure is essentially horizontally oriented, with an in-plane disorder of its lattice.

The morphology of these $(BABr)_x(CsPbBr_3)_{1-x}$ thin films was investigated using atomic force microscopy (AFM) (FigureS5, Supporting Information). There is a clear change in morphology of the thin films with increasing organic cation content, which follows a similar trend to the structural changes shown in Figure 2. For thin films of materials with $x = 0.17$ and 0.31, a uniform morphology composed of small grains is observed. For thin films with $x = 0.42$ and 0.5, similar morphologies are observed with several larger grains surrounded by very small, uniform grains. Despite the appearance of these larger grains, the root mean squared roughness of these films remains low ($R_q = 3.38$ nm ($x = 0.42$) and 3.98 nm ($x = 0.5$)). In these films, the

Table 1. Summary of representative device performance for $(BABr)_x(CsPbBr_3)_{1-x}$ light emitting diodes.

Perovskite composition	Max EQE_{EL} [%] @ bias	Max luminance [cd m^{-2}] @ bias	J @ max EQE_{EL} [mA cm^{-2}] @ bias	Turn-on Voltage [V] @ 0.1cd m^{-2}	EL peak @ max EQE_{EL}[nm]	FWHM of EL peak [nm]
$(BABr)_{0.17}(CsPbBr_3)_{0.83}$	2.20@4.6	5396@5.2	46.41@4.6	3.0	518	20.7
$(BABr)_{0.31}(CsPbBr_3)_{0.69}$	6.77@3.6	5270@5.0	6.35@3.6	3.0	515	21.7
$(BABr)_{0.42}(CsPbBr_3)_{0.58}$	12.91@3.0	3720@4.8	0.04@3.0	3.0	513	21.9
$(BABr)_{0.5}(CsPbBr_3)_{0.5}$	16.46@3.0	1685@5.4	0.01@3.0	3.0	507	23.7
$(BABr)_{0.58}(CsPbBr_3)_{0.42}$	4.19@3.2	58@5.6	0.03@3.2	3.0	495	28.9

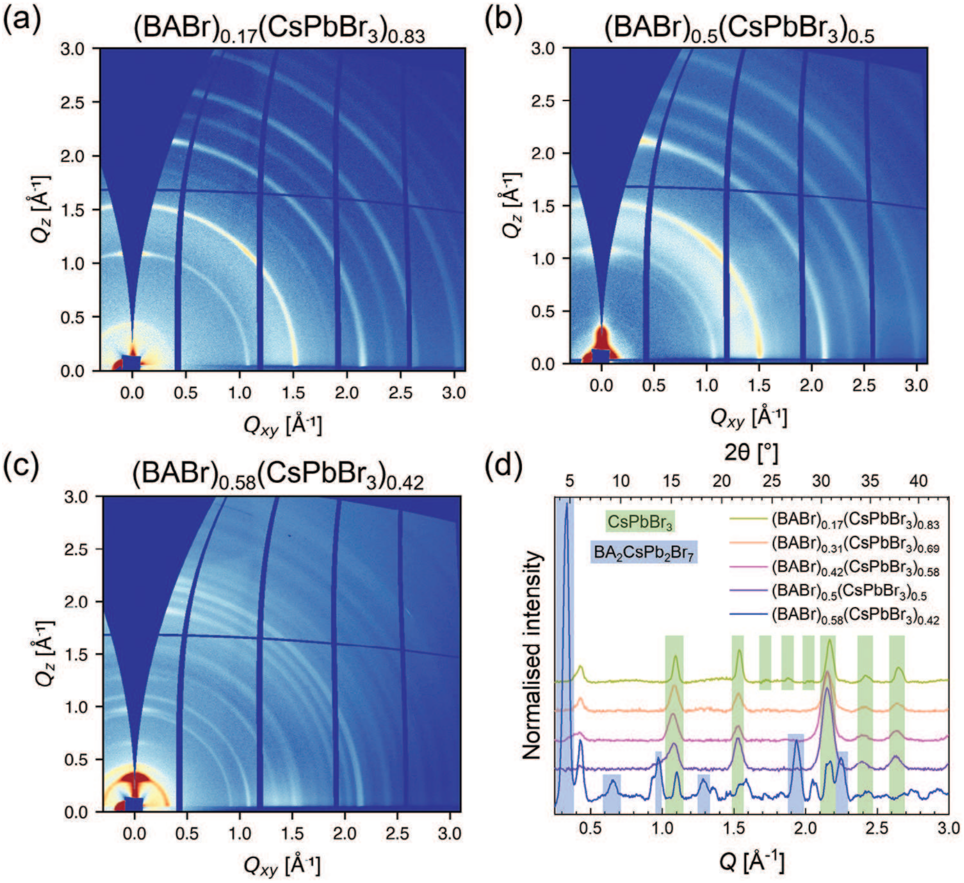

Figure 2. Grazing incidence wide angle X-ray scattering patterns (GIWAXS) of BABr-containing $CsPbBr_3$ films. 2D GIWAXS patterns from a) $(BABr)_{0.17}(CsPbBr_3)_{0.83}$, b) $(BABr)_{0.5}(CsPbBr_3)_{0.5}$ and c) $(BABr)_{0.58}(CsPbBr_3)_{0.42}$ films (remaining compositions are shown in Figure S3, Supporting Information). The Debye-Scherrer ring at Q ≈ 0.4 $Å^{-1}$ and broad ring at Q ≈1.3 $Å^{-1}$ are backgrounds from a polyimide window and epoxy substrate. d) 1D azimuthally integrated profiles of the 2D data for all compositions illustrating $CsPbBr_3$ in all cases, with additional peaks for the two highest concentrations and significant scattering intensity from $BA_2CsPb_2Br_7$ for the $x = 0.58$ composition. Additional 2D GIWAXS images prior to background subtraction are given in Figure S4 (Supporting Information).

majority of grains are uniform and smooth which results in the outliers appearing large; the low roughness values highlight that these large grains are not significant to film roughness. Another third morphological regime is observed for the composition with the highest organic cation content ($x = 0.58$). Here the thin film is composed of small (<100 nm) grains without any stark differences across the film surface. This change in morphology coincides with the changing structure, and deterioration of PeLED performance, for this composition $(BABr)_{0.58}(CsPbBr_3)_{0.42}$. Although significant, this change in morphology is unlikely to explain the trend in PeLED performance, thus we proceed to study the photophysical properties of the $(BABr)_x(CsPbBr_3)_{1-x}$ thin films.

Figure 3a shows absorbance and photoluminescence (PL) spectra for representative films of all compositions of $(BABr)_x(CsPbBr_3)_{1-x}$. Figures S6 and S7 (Supporting Information) show these plots independently for clarity. In both measurements, we observe a blue-shifting of the absorption onset and PL peak with increasing organic cation content. This correlates with the observed blue shift in the electroluminescence spectra of the PeLEDs. This blue-shifting of the absorption is concomitant with the absorption onset becoming shallower, indicative of increased electronic disorder. Taken together with the GIWAXS measurements in Figure 2 there is strong evidence that an increase in cation content results in an increase in both the structural and electronic disorder present within the thin films. The blue-shifting of the absorption onset and emission peak position suggest the presence of quantum confinement resulting from a reduction in the grain sizes within the film with increasing organic cation content. Clear evidence of absorption and emission from 2D perovskite structures is observed in $(BABr)_x(CsPbBr_3)_{1-x}$ thin films with $x = 0.5$ and 0.58 with peaks corresponding to the $n = 2$ $(BA_2CsPb_2Br_7)$ and $n = 3$ $(BA_2Cs_2Pb_3Br_{10})$ compositions.[37] The GIWAXS data (Figure 2) only shows clear evidence for the presence of 2D perovskite structures in the $x = 0.58$ composition, where the $n = 2$ $(BA_2CsPb_2Br_7)$ structure is observed. The lack of corresponding evidence for the $n = 3$ $(BA_2Cs_2Pb_3Br_{10})$ structure in the diffraction patterns for both $x = 0.5$ and $x = 0.58$, and $n = 2$ for $x = 0.5$, suggests that these structures are most likely present in very small domains which are not large enough to be detected by the diffraction measurements.[38] The blue-shifting

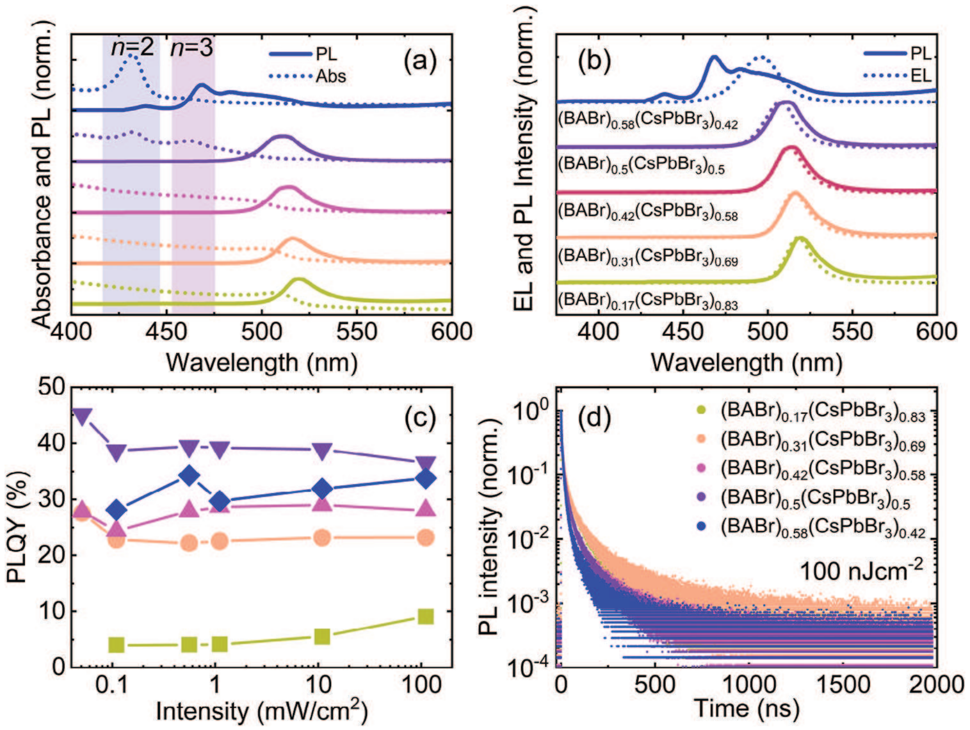

Figure 3. a) Absorbance (Abs) and photoluminescence (PL) spectra and b) electroluminescence (EL) and photoluminescence spectra, excited at 400 nm c) intensity-dependent photoluminescence quantum yield (PLQY) measurements, excited at 450 nm, and d) time-correlated single photon counting (TCSPC) measurements, excited at 400 nm (repetition rate 500 kHz) with a laser fluence of 100 nJcm^{-2} of representative thin films of $(\text{BABr})_x(\text{CsPbBr}_3)_{1-x}$ deposited on glass.

of the absorbance, photoluminescence, and electroluminescence spectra coupled with the thin film morphologies shown in the AFM images offer further evidence for very small grain sizes within the thin films, on the order of 10s of nanometers. The PL spectrum for thin films of $(\text{BABr})_{0.58}(\text{CsPbBr}_3)_{0.42}$ is broad, consisting of contributions from both a blue-shifted 3D CsPbBr_3 structure and the aforementioned 2D structures.[39] Whilst photoluminescence provides valuable insights into the charge-carrier properties of metal halide perovskite material. It is important to note that there is a significant difference in the processes occurring within a thin film under illumination compared to when it is being used as an emitting layer within an LED. In photoluminescence measurements, electron-hole pairs are generated within the bulk of the material and near each other spatially. Conversely, in electroluminescence measurements, electrons and holes are injected separately at opposite sides of the emissive layer. Therefore, it is important to compare the insights from each technique to gain a holistic understanding of the material's photophysical properties. Figure 3b compares the EL and PL spectra for all compositions. With the exception of $(\text{BABr})_{0.58}(\text{CsPbBr}_3)_{0.42,}$ the PL and EL character of all perovskite compositions are in close agreement with a very slight blue shifting of the EL relative to the PL, indicative of similar radiative recombination process under illumination or charge injection. The PL emission ranges from 517 nm ($x = 0.17$) to 495 nm ($x = 0.58$) matching the PeLED characteristics described earlier. The EL of $(\text{BABr})_{0.58}(\text{CsPbBr}_3)_{0.42}$ is strikingly different from its PL spectrum. Predominantly, the PeLED emission from this system appears to come from small 3D perovskite domains undetected in diffraction measurements, however there is a slight shoulder to the emission peak around 470 nm correlating to emission from $\text{BA}_2\text{Cs}_2\text{Pb}_3\text{Br}_{10}$ ($n = 3$). Conversely, the PL emission is broad, comprised of contributions from the $n = 2$, $n = 3$ and 3D perovskite which indicates that the emission pathways are substantially different for the $(\text{BABr})_{0.58}(\text{CsPbBr}_3)_{0.42}$ perovskite under illumination. This disparity between the PL and EL spectra indicates that the steady-state combined electron and hole density within the 2D phases following electronic charge injection is very low. To investigate the distribution of the 2D and 3D perovskite structures photoluminescence spectroscopy measurements were performed with the perovskite thin films excited from both the front and back side of the samples (Figure S8, Supporting Information). In compositions where there is clear evidence of 2D perovskite structures ($x = 0.5$ and 0.58) we observe little difference between the PL spectra when excited from the front (film) or back (substrate) side of the thin films. Conversely, for the $x = 0.17$ composition the PL signal when excited from the front side is blue-shifted relative to the backside. This suggests a lack of uniformity in the perovskite thin film structure resulting in a marginally wider bandgap material at the top perovskite surface compared to the perovskite thin film at the substrate interface.

To quantify the radiative efficiency of the perovskite compositions and to further understand the influence of the organic cation on the charge-carrier dynamics, intensity-dependent photoluminescence quantum yield (PLQY) and time-resolved photoluminescence measurements were carried out.

Figure 3c shows the intensity-dependent PLQY measurements of thin films of $(\text{BABr})_x(\text{CsPbBr}_3)_{1-x}$ on glass. All compositions, except for $x = 0.17$, show high PLQY values (>20%) across a wide range of intensities with only a small variation in the absolute PLQY value. The PLQY follows a similar trend to the EQE_{EL} of the PeLEDs with some slight differences. As the organic cation content increases up to $x = 0.5$ so does the PLQY, with the highest measured PLQY (45.1%) corresponding to the composition with the highest EQE_{EL} ($x = 0.5$). Once this critical point has been reached, additional organic cation content within the perovskite has a detrimental impact on the PLQY suggesting that past this compositional point the organic cation is starting to negatively impact the radiative efficiency of the perovskite thin films, consistent with the reduction in PeLED performance. A small variation in the absolute PLQY value across a broad range of intensities is generally indicative of charge-carrier recombination in the bimolecular regime (Figure S9, Supporting Information).[40] However, as will be discussed in more detail, we believe that the charge-carrier recombination studied in this work is excitonic in nature.

Figure 3d shows the transient PL decays, measured using time-correlated single photon counting (TCSPC), at a laser fluence of 100 nJcm^{-2}. Additional fluences and excitation wavelengths are shown in Figures S10 and S11 (Supporting Information) respectively. The transients were fit with stretched exponentials, full details are provided in the Supporting Information.[41] The PL transients, irrespective of fluence or wavelength, are composed of two distinct components: an initial fast decay at early times with a long decay tail. The radiative recombination rate for free carriers is expected to scale as a product of injected electron (n) and hole (p) number density, assuming equal photogeneration of electrons and holes, hence should increase as n^2 with increasing fluence. In contrast, radiative recombination of excitons is a “monomolecular” process, and the rate simply scales with absorbed photon density. The consequence in transient PL decays is that free-carrier recombination is expected to result in an increasing decay rate with increasing fluence, whereas exciton recombination should result in a decay rate insensitive to fluence, until very high fluence when exciton/exciton or exciton/free-carrier interactions start to become significant. We note that the rate of exciton formation from free carriers would be fluence dependent, however this process occurs on timescales that are too fast to be resolved in our experiment. For our material here, the fast decay component is approximately constant for all fluences. This observation in conjunction with the intensity-dependent PLQY studies, wherein no change in PLQY signal was observed with increasing excitation intensity (and therefore an increase in excited charge-carrier density), suggests that this early decay is related to the rapid recombination of excitons in the 3D perovskite structure. The long decay tail is most likely due to residual free carriers which, unlike excitons, need to travel through the perovskite to encounter their counterpart to recombine radiatively. The long decay tail has a shallow gradient and is fluence dependent as shown in Figures S10 and S11 (Supporting Information). This is denotative of slow non-radiative recombination and therefore long lifetimes for free charge carriers. Broadly this, in conjunction with the high PLQY values, indicates that the perovskite thin films are of a high quality, with a low trap density. Additionally, as the organic cation composition increases, the initial decay becomes faster, suggesting that a greater proportion of photogenerated carriers are bound excitons or rapidly relax into bound excitons. This suggests that as we add more organic cations, which result in 2D structure formation, the domains of the 3D perovskite get smaller resulting in quantum confinement and therefore higher exciton binding energies in the 3D perovskite structures. This was also consistent with the blue-shifted PL seen in Figure 3a. To differentiate between the contributions of the 2D and 3D perovskite structures to the charge-carrier dynamics, we repeated these measurements using a 470 nm laser excitation with a similar fluence (Figure S11, Supporting Information). This excitation wavelength was chosen as it is unable to excite the $n = 2$ and $n = 3$ 2D perovskite structures. For all compositions where $x > 0.17$ there is no change in the PL transients compared to those measured with a 400 nm excitation suggesting that the 2D structures are either not absorbing a significant fraction of the light, or any excitons formed in the 2D domains rapidly energy transfer to the 3D domains where they relax into the excitonic states of the 3D phase.

Transient absorption spectroscopy (TAS) was conducted on three compositions of the $(\text{BABr})_x(\text{CsPbBr}_3)_{1-x}$ quasi-2D heterostructure films to investigate the influence of the organic cation (BABr) on the charge-carrier dynamics occurring in these materials. Figures S12–S14 (Supporting Information) show the 2D maps of TA transients as a function of delay and wavelength. When the organic cation component x was 0.17, the ground state bleach (GSB) was centered at 510 nm, suggesting that this GSB signature is mainly dominated by the 3D phase. As x was increased to 0.5, a notable blue shift of the GSB to 500 nm was observed, suggesting that the more quantum confined 2D/3D phase had been formed. When x was further increased to 0.58, a broader GSB centered at 510 nm was observed. This implies the coexistence of a range of 2D and 3D phases, consistent with the photoluminescence and absorption measurements. Experimental limitations did not allow us to monitor the photobleached associated with the wider bandgap phases in the UV region, however, the dynamics of the 3D phase provides a good indication of transfer mechanisms. To investigate the charge transfer process from 2D to 3D phases, we fitted TA transients for each composition at the wavelength of 510 nm with a stretched exponential function, i.e. using the function

$$\frac{\Delta T}{T} = Ae^{\left(-\frac{t}{\tau}\right)^{\beta}} \tag{1}$$

where A is the amplitude, τ is the lifetime, β is the stretched exponent and t is the delay.

As apparent from the fits in Figures S15–S17 (Supporting Information), and the extracted fitting parameters listed in Table S2 (Supporting Information), when x was increased from 0.17 to 0.5, the lifetime (τ) increased from 132 ± 2 ps to 162 ± 8 ps. This substantial increase in τ can be attributed to the charge-carrier transfer from the $n = 2$ and $n = 3$ 2D phases to the 3D phase as such charge-carrier feeding results in an apparent delay in the decay of charge-carrier density in the 3D phase.[42] The slight increase in τ between $x = 0.5$ and $x = 0.58$ suggests that an

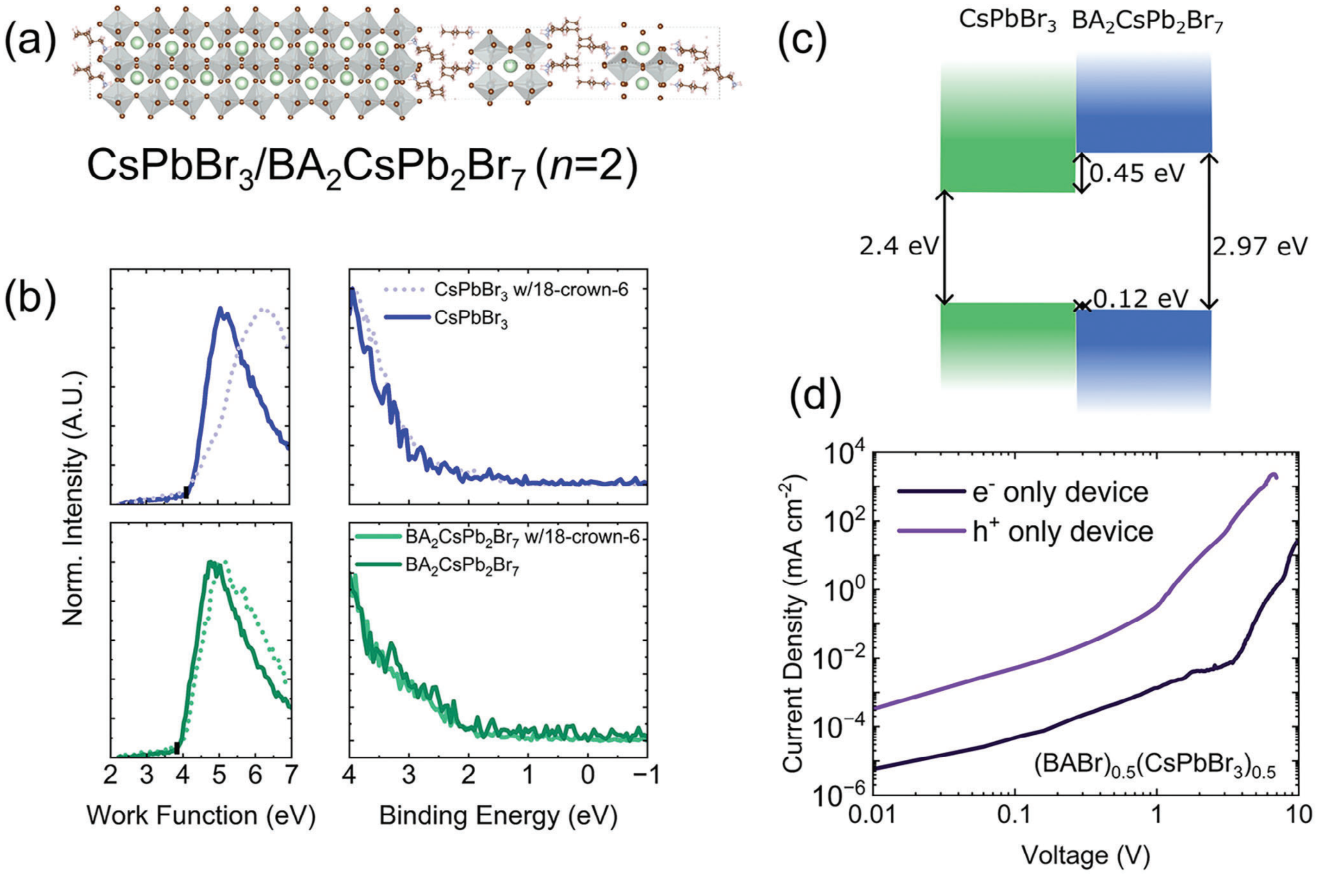

Figure 4. a) 2D/3D heterostructure model composed of $CsPbBr_3$ interfaced with $BA_2CsPb_2Br_7$ (see Supporting Information for details) b) Ultraviolet photoelectron spectroscopy (UPS) measurements of thin films of model systems $CsPbBr_3$ and $BA_2CsPb_2Br_7$ on ITO glass with and without the 18-crown-6 additive used in this work. c) representative energy level diagrams of 2D/3D heterostructure interface constructed using the valence band positions extracted using linear fitting of the UPS and measured optical bandgaps from absorbance measurements and d) unipolar charge carrier injection measurements for $BABr_{0.5}(CsPbBr_3)_{0.5}$.

analogous charge-carrier transfer mechanism from the 2D phase to the 3D phase is responsible for the prolonged τ within the 3D phase. We highlight that the timescale probed by our experiment is not affected by differences in the first-order defect-assisted recombination, which can vary from sample to sample because of fluctuations in crystallinity and defect density.

The role of the organic cation must extend beyond inducing quantum confinement since confinement alone could not explain the trend in PeLED performance observed. The negative impact of high levels of organic cation in terms of device performance is significant whereas the photoluminescence measurements do not suggest a large detrimental change in charge-carrier dynamics and recombination when we add the highest content of 2D forming cations.

To study the influence of cation content on the inherent energy level alignment of the composite thin films, ultraviolet photoelectron spectroscopy (UPS) measurements were carried out on thin films of the perovskite on ITO glass. The data and fits used to extract the valence band energy and work function are shown in Figures S18–S20 and Tables S3 and S4 (Supporting Information). Where the presence of the $n = 2$ ($BA_2CsPb_2Br_7$) and $n = 3$ ($BA_2Cs_2Pb_3Br_{10}$) structures has been observed for a specific composition, there is a resulting deepening of the measured valence band energy. This is perhaps unsurprising since the $n = 2$ ($BA_2CsPb_2Br_7$) and $n = 3$ ($BA_2Cs_2Pb_3Br_{10}$) structures have been previously reported as possessing wide bandgaps 2.97 eV ($n = 2$) and 2.77 eV ($n = 3$).[37] The complex nature of these heterostructures makes it difficult to deconvolute the influence of the various compositions on the electronic structure of the perovskite emitter. We, therefore, investigated thin films of $CsPbBr_3$, BA_2PbBr_4, and $BA_2CsPb_2Br_7$ as model systems, to develop an understanding of the energetic landscape within the perovskite emitting layer in the PeLEDs. We investigated these systems with and without the 18-crown-6 used in the perovskite fabrication in this work, to facilitate comparison to literature reports, and using both the linear and logarithmic fitting methods seen in **Figure 4**b and Figures S21–S23 (Supporting Information). Our measured valence band maxima and bandgap for $CsPbBr_3$ align with those reported in the literature.[43,44] Conversely, our measured valence band maxima for BA_2PbBr_4 (Figure S22 and Table S4, Supporting Information) are significantly different from those reported by Silver and co-workers however our thin films are fabricated significantly differently and we believe that this accounts for these differences.[45] Absorbance and photoluminescence spectra corresponding to these model systems can be found in Figures S24–S25 (Supporting Information). We observe small offsets between the measured valence band positions of $CsPbBr_3$ and $thBA_2CsPb_2Br_7$ 2D structure Figure 4c. Due to the significant difference in bandgap between the 2D and the 3D perovskite structures, the close alignment of the valence band positions suggests that the majority of the energy level misalignment is occurring between the conduction bands of the $CsPbBr_3$ and the 2D perovskite structure. Such a situation presents a barrier to electron transport across a 2D/3D heterostructure as we illustrate in the energy level schematic shown in Figure 4c. Indeed, from a DFT calculation performed on the 2D/3D heterostructure model represented in Figure 4c (see Supporting Information for details), we found a small energy difference of 0.1–0.2 eV between the valence band electronic states in the 2D ($n = 2$) and 3D regions (Figure S26, Supporting Information). Interestingly, this difference increases when separated 2D ($n = 2$) and 3D slabs are considered in the simulation (Figure S27, Supporting Information). We attribute this to surface dipole compensation at the interface between the two regions of the 2D/3D heterostructures, an effect already observed in the simulation of iodine-based 2D/3D heterostructures.[46]

To confirm the above band alignments and examine potential barriers to charge injection and transport within our various perovskite emitter compositions we fabricated unipolar diodes and performed unipolar current injection measurements. Devices with the following architectures were fabricated for the respective charge-carrier types: electron-only devices (ITO/ZnMgO nanoparticles/perovskite/TPBi/LiF/Al) and hole only devices (ITO/PEDOT:PSS/PVK/perovskite/MoO_3/Ag). Figure 4d shows representative characteristics of electron and hole-only devices incorporating the best performing composition ($x = 0.5$). Devices related to additional compositions can be found in Supplementary Figure S28 (Supporting Information). For the electron-only devices, we observe a current density at least one order of magnitude lower than that observed in the corresponding hole-only devices. This suggests that the injection of electrons into this perovskite is particularly challenging and may be indicative of a higher density of electron traps compared to hole traps in the perovskite or at the interfaces. These unipolar charge injection measurements confirm a significant barrier to electron injection and/or transport as suggested by the UPS measurements.

It is clear from our results that there is a strong correlation between the formation of regions of crystalline 2D perovskite and a reduction in PeLED device performance. Ultraviolet photoelectron spectroscopy measurements and single carrier devices present strong evidence that the observed 2D structures dispersed throughout the perovskite films result in a significant barrier to electron injection. The performance of corresponding PeLEDs supports this notion, with a reduction in current density and an increase in required turn-on voltage observed with these 2D structures. This together suggests that crystalline 2D regions present a significant barrier to charge injection.

3. Conclusion

In this work, we have studied the effect of increased 2D perovskite components in quasi-2D perovskite light-emitting diodes. Using AFM and X-ray scattering techniques, we identified that the 2D component results in a reduction in grain-size which corresponds to a concomitance blue-shift in the PL peak position. The dramatic reduction in performance from the highest 2D component $(BABr)_{0.58}(CsPbBr_3)_{0.42}$ can be explained by a small drop in PLQY and a substantial electron injection/transport barrier, confirmed by photoelectron spectroscopy, induced by crystalline Ruddlesden–Popper phases which first appear at this composition. To increase the performance of quasi-2D PeLEDs further, the field must suppress the formation of crystalline 2D perovskite within the emitter layer whilst promoting the growth of structures that passivate traps. Furthermore, improving the electron injection contact, to enable direct injection into the 2D structures, is likely to be an important area of future research.

Supporting Information

Supporting Information is available from the Wiley Online Library or from the author.

Acknowledgements

A.J.R. and W.H.J. contributed equally to this work. The authors acknowledge funding from the European Union's Horizon 2020 research and innovation program under grant agreement No. 861985 (PEROCUBE), the Engineering and Physical Sciences Research Council (EP/T012455/1), and (EP/T025077/1). This work was supported by the National Research Foundation of Korea (NRF-2022H1D3A3A01077343, 2022R1A2C4002248, 2021M3H4A1A02049006, and 2022M3H4A1A03076093). R.D.J.O. and A.D. acknowledge funding from the Penrose Scholarship. J.E. acknowledges the financial support from the Institut Universitaire de France. This work was granted access to the HPC resources of TGCC under the allocations 2022- A0130907682 and 2022- A0120911434 made by GENCI. The GIWAXS experiments were performed on beamline BM28–XMaS at the European Synchrotron Radiation Facility (ESRF), Grenoble, France as part of proposal A28-1/1313. The authors are grateful to Oier Bikondoa at the ESRF and Irfan Habib for providing assistance in acquiring the data. J.J. and C.K. are grateful to Boubacar Traoré and Mikaël Képénékian for useful advices related to the DFT simulations.

Conflict of Interest

H.J.S. is Co-Founder, Director, and Chief Scientific Officer of Helio Display Materials Ltd.

Data Availability Statement

The data that support the findings of this study are openly available in ORDA at 10.15131/shef.data.23946990.

Keywords

2D/3D perovskites, butylammonium, electronic structure, heterostructure, light-emitting diodes

Received: August 14, 2023
Revised: November 27, 2023

---

[1] A. Fakharuddin, M. K. Gangishetty, M. Abdi-Jalebi, S.-H. Chin, A. R. Bin Mohd Yusoff, D. N. Congreve, W. Tress, F. Deschler, M. Vasilopoulou, H. J. Bolink, *Nat. Electron.* **2022**, *5*, 203.

[2] X.-K. Liu, W. Xu, S. Bai, Y. Jin, J. Wang, R. H. Friend, F. Gao, *Nat. Mater.* **2021**, *20*, 10.

[3] M. Vasilopoulou, A. Fakharuddin, F. P. García De Arquer, D. G. Georgiadou, H. Kim, A. R. B. Mohd Yusoff, F. Gao, M. K. Nazeeruddin, H. J. Bolink, E. H. Sargent, *Nat. Photon.* **2021**, *15*, 656.

[4] Z.-K. Tan, R. S. Moghaddam, M. L. Lai, P. Docampo, R. Higler, F. Deschler, M. Price, A. Sadhanala, L. M. Pazos, D. Credgington, F. Hanusch, T. Bein, H. J. Snaith, R. H. Friend, *Nat. Nanotechnol.* **2014**, *9*, 687.

[5] M. Era, S. Morimoto, T. Tsutsui, S. Saito, *Appl. Phys. Lett.* **1994**, *65*, 676.

[6] D. Yang, B. Zhao, T. Yang, R. Lai, D. Lan, R. H. Friend, D. Di, *Adv. Funct. Mater.* **2022**, *32*, 2109495.

[7] J. S. Kim, J.-M. Heo, G.-S. Park, S.-J. Woo, C. Cho, H. J. Yun, D.-H. Kim, J. Park, S.-C. Lee, S.-H. Park, E. Yoon, N. C. Greenham, T.-W. Lee, *Nature* **2022**, *611*, 688.

[8] K. Ji, M. Anaya, A. Abfalterer, S. D. Stranks, *Adv. Opt. Mater.* **2021**, *9*, 2002128.

[9] L. Protesescu, S. Yakunin, M. I. Bodnarchuk, F. Krieg, R. Caputo, C. H. Hendon, R. X. Yang, A. Walsh, M. V. Kovalenko, *Nano Lett.* **2015**, *15*, 3692.

[10] Y.-H. Kim, H. Cho, J. H. Heo, T.-S. Kim, N. Myoung, C.-L. Lee, S. H. Im, T.-W. Lee, *Adv. Mater.* **2015**, *27*, 1248.

[11] S. Kumar, J. Jagielski, N. Kallikounis, Y.-H. Kim, C. Wolf, F. Jenny, T. Tian, C. J. Hofer, Y.-C. Chiu, W. J. Stark, T.-W. Lee, C.-J. Shih, *Nano Lett.* **2017**, *17*, 5277.

[12] Y. Liu, Z. Yu, S. Chen, J. H. Park, E. D. Jung, S. Lee, K. Kang, S.-J. Ko, J. Lim, M. H. Song, B. Xu, H. J. Snaith, S. H. Park, B. R. Lee, *Nano Energy* **2021**, *80*, 105511.

[13] C. Sun, Y. Jiang, M. Cui, L. Qiao, J. Wei, Y. Huang, L. Zhang, T. He, S. Li, H.-Y. Hsu, C. Qin, R. Long, M. Yuan, *Nat. Commun.* **2021**, *12*, 2207.

[14] Z. Wang, F. Wang, W. Sun, R. Ni, S. Hu, J. Liu, B. Zhang, A. Alsaed, T. Hayat, Z. Tan, *Adv. Funct. Mater.* **2018**, *28*, 1804187.

[15] Z. Ren, L. Li, J. Yu, R. Ma, X. Xiao, R. Chen, K. Wang, X. W. Sun, W.-J. Yin, W. C. H. Choy, *ACS Energy Lett.* **2020**, *5*, 2569.

[16] P. Vashishtha, M. Ng, S. B. Shivarudraiah, J. E. Halpert, *Chem. Mater.* **2019**, *31*, 83.

[17] C. Katan, N. Mercier, J. Even, *Chem. Rev.* **2019**, *119*, 3140.

[18] Y. Chen, Y. Sun, J. Peng, J. Tang, K. Zheng, Z. Liang, *Adv. Mater.* **2018**, *30*, 1703487.

[19] Z. Chu, Y. Zhao, F. Ma, C.-X. Zhang, H. Deng, F. Gao, Q. Ye, J. Meng, Z. Yin, X. Zhang, J. You, *Nat. Commun.* **2020**, *11*, 4165.

[20] W. Xiong, C. Zou, W. Tang, S. Xing, Z. Wang, B. Zhao, D. Di, *ACS Energy Lett.* **2023**, *8*, 2897.

[21] S. Liu, Z. Guo, X. Wu, X. Liu, Z. Huang, L. Li, J. Zhang, H. Zhou, L.-D. Sun, C.-H. Yan, *Adv. Mater.* **2023**, *35*, 2208078.

[22] B. Wang, Y.-H. Zhou, S. Yuan, Y.-H. Lou, K.-L. Wang, Y. Xia, C.-H. Chen, J. Chen, Y.-R. Shi, Z.-K. Wang, L.-S. Liao, *Angew. Chem., Int. Ed.* **2023**, *62*, e202219255.

[23] Y. Jiang, M. Cui, S. Li, C. Sun, Y. Huang, J. Wei, L. Zhang, M. Lv, C. Qin, Y. Liu, M. Yuan, *Nat. Commun.* **2021**, *12*, 336.

[24] J. Jiang, Z. Chu, Z. Yin, J. Li, Y. Yang, J. Chen, J. Wu, J. You, X. Zhang, *Adv. Mater.* **2022**, *34*, 2204460.

[25] L. Zhang, N. Li, D. Liu, G. Tao, W. Xu, M. Li, Y. Chu, C. Cao, F. Lu, C. Hao, J. Zhang, Y. Cao, F. Gao, N. Wang, L. Zhu, W. Huang, J. Wang, *Angew. Chem., Int. Ed.* **2022**, *61*, e202209337.

[26] Y. Miao, L. Cheng, W. Zou, L. Gu, J. Zhang, Q. Guo, Q. Peng, M. Xu, Y. He, S. Zhang, Y. Cao, R. Li, N. Wang, W. Huang, J. Wang, *Light Sci. Appl.* **2020**, *9*, 89.

[27] Y. Sun, L. Ge, L. Dai, C. Cho, J. Ferrer Orri, K. Ji, S. J. Zelewski, Y. Liu, A. J. Mirabelli, Y. Zhang, J.-Y. Huang, Y. Wang, K. Gong, M. C. Lai, L. Zhang, D. Yang, J. Lin, E. M. Tennyson, C. Ducati, S. D. Stranks, L.-S. Cui, N. C. Greenham, *Nature* **2023**, *615*, 830.

[28] S.-J. Woo, J. S. Kim, T.-W. Lee, *Nat. Photon.* **2021**, *15*, 630.

[29] A. Fakharuddin, W. Qiu, G. Croes, A. Devizis, R. Gegevicius, A. Vakhnin, C. Rolin, J. Genoe, R. Gehlhaar, A. Kadashchuk, V. Gulbinas, P. Heremans, *Adv. Funct. Mater.* **2019**, *29*, 1904101.

[30] A. Giuri, Z. Yuan, Y. Miao, J. Wang, F. Gao, N. Sestu, M. Saba, G. Bongiovanni, S. Colella, C. Esposito Corcione, G. Gigli, A. Listorti, A. Rizzo, *Sci. Rep.* **2018**, *8*, 15496.

[31] S. Lee, J. H. Park, B. R. Lee, E. D. Jung, J. C. Yu, D. Di Nuzzo, R. H. Friend, M. H. Song, *J. Phys. Chem. Lett.* **2017**, *8*, 1784.

[32] J. H. Warby, B. Wenger, A. J. Ramadan, R. D. J. Oliver, H. C. Sansom, A. R. Marshall, H. J. Snaith, *ACS Nano* **2020**, *14*, 8855.

[33] S. Sidhik, Y. Wang, M. De Siena, R. Asadpour, A. J. Torma, T. Terlier, K. Ho, W. Li, A. B. Puthirath, X. Shuai, A. Agrawal, B. Traore, M. Jones, R. Giridharagopal, P. M. Ajayan, J. Strzalka, D. S. Ginger, C. Katan, M. A. Alam, J. Even, M. G. Kanatzidis, A. D. Mohite, *Science* **2022**, *377*, 1425.

[34] X. Zhao, T. Liu, Q. C. Burlingame, T. Liu, R. Holley, G. Cheng, N. Yao, F. Gao, Y.-L. Loo, *Science* **2022**, *377*, 307.

[35] J. Jae Do, Y. Chung, K. S. Kim, D. H. Kim, J. W. Jung, *J. Alloys Compd.* **2023**, *940*, 168913.

[36] E. Cohen, A. Nagel, M. Fouchier, L. Popilevsky, Y. Kauffmann, S. Khalfin, S. Dror, Y. Bekenstein, *Chem. Mater.* **2022**, *34*, 5377.

[37] H. Chen, J. Lin, J. Kang, Q. Kong, D. Lu, J. Kang, M. Lai, L. N. Quan, Z. Lin, J. Jin, L.-W. Wang, M. F. Toney, P. Yang, *Sci. Adv.* **2020**, *6*, eaay4045.

[38] B. Zhao, Y. Lian, L. Cui, G. Divitini, G. Kusch, E. Ruggeri, F. Auras, W. Li, D. Yang, B. Zhu, R. A. Oliver, J. L. Macmanus-Driscoll, S. D. Stranks, D. Di, R. H. Friend, *Nat. Electron.* **2020**, *3*, 704.

[39] E. S. Parrott, J. B. Patel, A.-A. Haghighirad, H. J. Snaith, M. B. Johnston, L. M. Herz, *Nanoscale* **2019**, *11*, 14276.

[40] M. B. Johnston, L. M. Herz, *Acc. Chem. Res.* **2016**, *49*, 146.

[41] D. C. Johnston, *Phys. Rev. B* **2006**, *74*, 184430.

[42] M. Righetto, D. Giovanni, S. S. Lim, T. C. Sum, *Appl. Phys. Rev.* **2021**, *8*, 011318.

[43] A. J. Ramadan, M. Ralaiarisoa, F. Zu, L. A. Rochford, B. Wenger, N. Koch, H. J. Snaith, *Chem. Mater.* **2020**, *32*, 114.

[44] J. Endres, D. A. Egger, M. Kulbak, R. A. Kerner, L. Zhao, S. H. Silver, G. Hodes, B. P. Rand, D. Cahen, L. Kronik, A. Kahn, *J. Phys. Chem. Lett.* **2016**, *7*, 2722.

[45] S. Silver, J. Yin, H. Li, J.-L. Brédas, A. Kahn, *Adv. Energy Mater.* **2018**, *8*, 1703468.

[46] B. Traoré, P. Basera, A. J. Ramadan, H. J. Snaith, C. Katan, J. Even, *ACS Energy Lett.* **2022**, *7*, 349.